Target Current Modulation as a Novel Approach for Active Balancing in Automotive MMSPCs

1st Tobias Merz*, 2nd Nils Hellmann, 3rd Eduard Specht, 4th Marc Hiller
Elektrotechnisches Institut (ETI)
Karlsruhe Institute of Technology (KIT)
Karlsruhe, Germany
*E-mail: tobias.merz@kit.edu

***Abstract*—A main challenge in the use of an automotive Modular Multilevel Series Parallel Converter (MMSPC) is combining high efficient operation alongside active balancing of the distributed batteries. To overcome this challenge a new modulation method is introduced. The aim of Target Current Modulation (TCM) is to have a high utilization of the total energy stored in the batteries and therefore, an extended range of the powered electric vehicle (EV). The TCM algorithm calculates an optimal switching state of the MMSPC to achieve a current distribution among the single modules which fits best the precalculated target currents for each battery. These target currents are a combination of a loss optimal current distribution and offset currents that are added to fulfill side conditions such as state of charge (SoC) balancing. Feasible battery current distributions are calculated by a model-predictive approach and evaluated in each control cycle. TCM is implemented on a field-programmable gate array (FPGA) and tested with a standardized automotive driving cycle on a test bench.**

***Index Terms*—Target Current Modulation, Multilevel Converters, Automotive, Model Prediction, Real-Time, Battery Management System, Active Balancing, Cascaded H-Bridge, Integrated Batteries**

I. Introduction

Since Modular Multilevel Converter (MMC) and related modular topologies were introduced [1], they have been under detailed investigation for different applications like grid coupling and STATCOMs [2], [3], energy storage systems [4], [5] and motor drives [6], [7]. Concerning magnetic losses, dielectric stress and system efficiency, MMC topologies with additional parallel states, like the modular multilevel series parallel converter (MMSPC) offer advantages over conventional two-level converters for automotive applications [8]–[10]. Still, they are under further investigation to proof stable and reliable operation over the full operational range. However, one drawback of the MMSPC topology is that simple, sorting based state of charge (SoC) balancing algorithms can not be applied [11]. Instead, more complex and computationally intensive algorithms are needed. Therefore, several algorithms with different approaches have been developed to consider active SoC balancing explicitly [12]–[17] or implicitly [18]. Next to active balancing, the degrees of freedom of an MMSPC can be used to reduce power loss of the converter and increase the range of the electric vehicles (EV). In the following, a new algorithm for an automotive MMSPC that combines different objectives like high efficient operation and balancing of the SoCs or the battery temperatures is described. This specific modulation algorithm, which is called Target Current Modulation (TCM) is able to evaluate the optimal next switching state of the MMSPC within each control period in real-time. As a result and in comparison to the state of the art, TCM leads to a higher driving range of an EV with an MMSPC as main power converter due to a better utilization of the energy stored in the batteries. However, TCM only optimizes the internal switching states of the converter, the overlaid PI-controllers for motor speed and torque of the used automotive drive are not affected and can be replaced by other, more sophisticated control algorithms.

II. Topology and Operation

The topology under investigation, is an MMSPC with asymmetric submodules (SM) as shown in Fig. 1a. Each phase consists of an equal count n_{ph} of SMs, and they are connected as shown in Fig. 1b. The key feature of the MMSPC topology is that SMs which are not needed in a series state to provide the required output voltage (series-positive or series-negative), can be switched in a parallel state to its adjacent SM. These additional parallel states can be used for both reduced ohmic losses of the converter and active balancing of the SoCs, due to better distributed currents. The topology and the main operation principle is explained in more detail in [11].

III. Target Current modulation

It is shown in [17] that the combination of precise current estimation with an additional usage of the common-mode (CM) voltage U_{CM} leads to either reduced losses or SoC balancing, whereas the focus on only one of these objectives results either in uncontrolled spreading of the SoCs or higher losses, respectively. On top of that, the combination of these conflicting objectives with weighting factors is arbitrary because of the different physical units of power losses (in watts) and a difference in SoC (in percentage points %P of the total charge). Therefore the TCM approach is used to combine high efficient operation with SoC balancing implicitly. In addition, other objectives like temperature balancing can be added.

The block diagram depicted in Fig. 2 gives an overview of the location and the input and output signals of the TCM block. It is implemented on the signal processing system of the MMSPC which is an field-programmable gate array

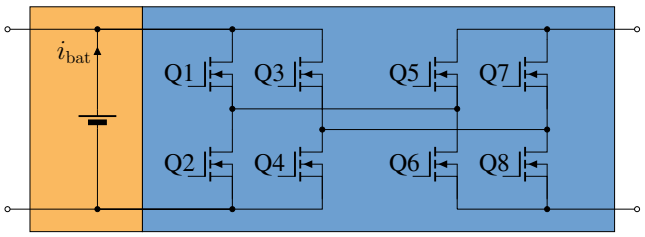

(a) Micro topology: Asymmetric SM

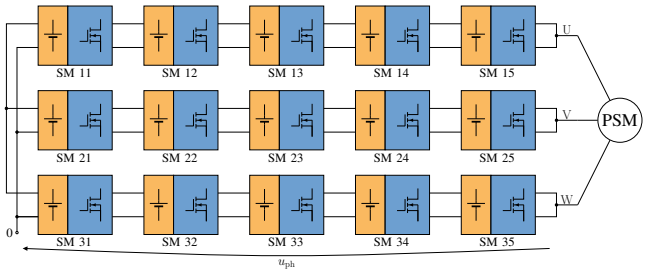

(b) Macro topology with $n_{\mathrm{ph}} = 5$

Fig. 1: MMSPC Micro and Macro Topology

(FPGA). On signal flow level it is located after the current controllers and the delta-sigma modulators (DSM) to avoid any interaction with the controllers and to be easily replaceable by other modulation methods. Besides the required discrete output level per phase $\vec{l}_{\mathrm{DSM}} = [l_{\mathrm{U}}, l_{\mathrm{V}}, l_{\mathrm{W}}]^T$ with $l_X \in \{-(n_{\mathrm{ph}}-1), ..., 0, ..., n_{\mathrm{ph}}\}$ and the d/q current setpoints $i_{\mathrm{d,sp}}$ and $i_{\mathrm{q,sp}}$, other measured or estimated quantities of the system are required, including the measured phase currents $\vec{i}_{\mathrm{ph}} = [i_{\mathrm{U}}, i_{\mathrm{V}}, i_{\mathrm{W}}]^T$, the SoCs of the individual SMs as well as the motor speed n_{machine}. In addition, other operating factors of the system, summarized as miscellaneous (misc), can be taken into account. The output of the TCM block is the optimal switching vector $\vec{s}_{\mathrm{opt}}$, which leads to the best result of the internal calculation process.

Internally, TCM works with battery target currents $\boldsymbol{i}_{\mathrm{target}}$ which is eponymous for the modulation scheme. These target currents are composed of several parts. An ohmic loss minimal current distribution $\boldsymbol{i}_{\mathrm{efficiency}}$ together with additional offset currents $\boldsymbol{i}_{\mathrm{offset}}$ to achieve other objectives are calculated in each modulation step in real-time. Due to the multiple degrees of freedom to choose the switching states of the MMSPC, possible battery currents $\boldsymbol{i}_{\mathrm{bat,pred}}$ are predicted [17] and compared to the target currents $\boldsymbol{i}_{\mathrm{target}}$ as explained in Section III-F. Fig. 3 shows the internal structure of the TCM-block. Each block will be explained in the following subsections.

Each matrix used in this contribution is indicated in bold letters. Since the MMSPC is used in a three-phase system, each matrix has the dimension of $3 \times n_{\mathrm{ph}}$. For each of the SMs, an individual target battery current $i_{\mathrm{target},pm}$ is specified. The index $p \in \{1 \equiv U, 2 \equiv V, 3 \equiv W\}$ defines the phase and $m \in \{1, ..., n_{\mathrm{ph}}\}$ is the number of the SM within the phase. The SM with index $m = 1$ is the module at the neutral point of the MMSPC and $m = n_{\mathrm{ph}}$ indicates the SM that is closest to the machine.

A. Efficiency

In the efficiency block, an optimal (i.e. loss minimal) current distribution $\boldsymbol{i}_{\mathrm{efficiency}}$ is determined based on the required discrete output levels $\vec{l}_{\mathrm{DSM}}$ of the DSMs and the phase currents $\vec{i}_{\mathrm{ph}}$. This is shown in (1).

$$\boldsymbol{i}_{\mathrm{efficiency}} = f_{i,\mathrm{efficiency}}(\vec{l}_{\mathrm{DSM}}, \vec{i}_{\mathrm{ph}}) \tag{1}$$

This current distribution is the result of an optimization for minimal ohmic losses in both the semiconductors and the batteries of the system according to the mathematical model explained in [17]. Here, all degrees of freedom of the MMSPC, especially the CM voltage, are used. The ohmic losses $P_{\mathrm{L,R}}$ are calculated according to (2) from the equivalent resistances of the respective phase $R_{\mathrm{ph},p}$ and the phase currents $\vec{i}_{\mathrm{ph}}$.

$$P_{\mathrm{L,R}} = R_{\mathrm{ph,U}} i_{\mathrm{ph,U}}^2 + R_{\mathrm{ph,V}} i_{\mathrm{ph,V}}^2 + R_{\mathrm{ph,W}} i_{\mathrm{ph,W}}^2 \tag{2}$$

However, this calculation scheme is only valid under the assumption that the batteries that are switched in parallel have an identical output voltage U_{bat} and thus no equalizing current. Equalizing currents place an additional load on the batteries and consequently lead to further losses. This simplification holds, since the batteries are balanced actively during operation.

B. SoC Balancing

The goal of the SoC balancing block is to equalize the SoCs of the distributed batteries. It is pursued by reducing the load on less charged batteries and increasing the load on more charged batteries taking the setpoint currents $i_{\mathrm{d,sp}}$ and $i_{\mathrm{q,sp}}$ into account. This target current modification is represented by the balancing offset currents $\boldsymbol{i}_{\mathrm{offset,bal}}$. They are calculated with the respective deviation between the SoC of the SM at position pm and the arithmetic mean of all SoCs $\overline{SoC}$ (see (3)).

$$\overline{SoC} = \frac{1}{3n_{\mathrm{ph}}} \sum_{p=1}^{3} \sum_{m=1}^{n_{\mathrm{ph}}} SoC_{pm} \tag{3}$$

To normalize these balancing offset currents, a dynamic scaling factor $d_{\overline{SoC}}(\boldsymbol{SoC})$ is used. This scaling factor is the mean absolute deviation of all SoCs. The calculation can be seen in (4). To prevent division by zero, the auxiliary variable a is introduced to limit the reciprocal of $d_{\overline{SoC}}(\boldsymbol{SoC})$ in (6). Additionally, the limit a_{lim} is used to set the level when the SoCs are sufficiently balanced and the impact of balancing is reduced (e.g. $a_{\mathrm{lim}} = 0.1$). The mathematical description of the auxiliary variable a can be seen in (5).

$$d_{\overline{SoC}}(\boldsymbol{SoC}) = \frac{1}{3n_{\mathrm{ph}}} \sum_{p=1}^{3} \sum_{m=1}^{n_{\mathrm{ph}}} |SoC_{pm} - \overline{SoC}| \tag{4}$$

$$a = \begin{cases} d_{\overline{SoC}}(\boldsymbol{SoC}) & \text{if } d_{\overline{SoC}}(\boldsymbol{SoC}) > a_{\mathrm{lim}} \\ a_{\mathrm{lim}} & \text{if } d_{\overline{SoC}}(\boldsymbol{SoC}) \leq a_{\mathrm{lim}} \end{cases} \tag{5}$$

To obtain currents from the normalized deviation, a multiplication with the magnitude of the setpoint vector in d/q coordinates is performed. In (6) the calculation of each module

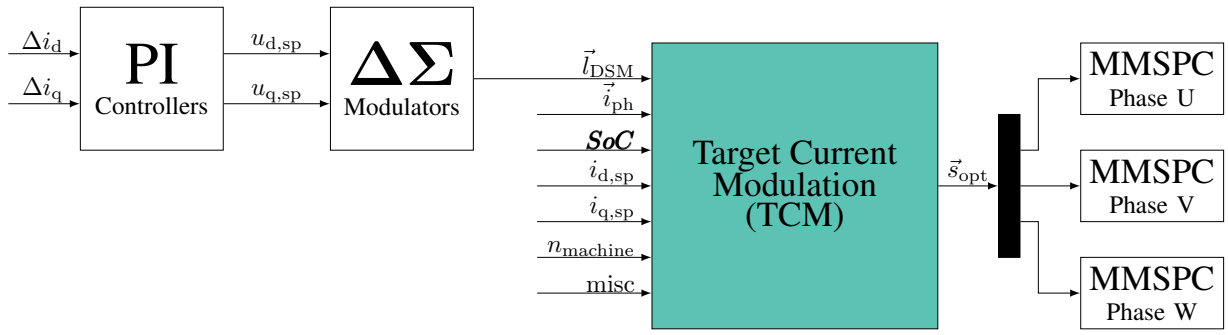

Fig. 2: Simplified block diagram of TCM's logical location

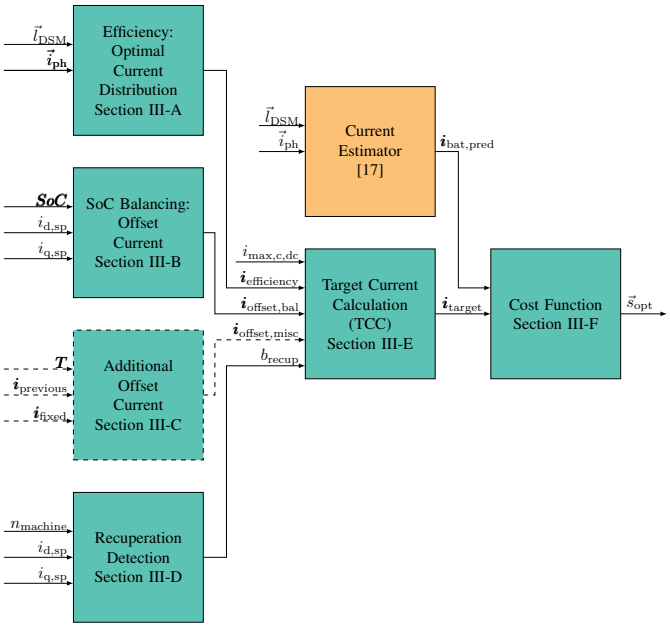

Fig. 3: Block diagram of the internal structure TCM algorithm

offset current $i_{\mathrm{offset,bal},pm}$ of the matrix $\boldsymbol{i}_{\mathrm{offset,bal}}$ can be seen. The factor g_bal determines the speed of convergence of the balancing. The higher the value of g_bal the faster the SoCs equalize, whereas the efficiency during the convergence is lower. As soon as the SoCs are balanced, the effect of these balancing offset current can be neglected since the deviation of the SoCs vanishes.

$$i_{\mathrm{offset,bal},pm} = \frac{1}{a}(SoC_{pm} - \overline{SoC}) \cdot \sqrt{i_\mathrm{q,sp}^2 + i_\mathrm{d,sp}^2} \cdot g_\mathrm{bal} \quad (6)$$

C. Additional Offset Currents

With TCM, additional offset current blocks can be implemented easily. Similar to the SoC balancing, miscellaneous offset currents $\boldsymbol{i}_{\mathrm{offset,misc}}$ can be determined. Based on the measured temperatures $\boldsymbol{T}$ of the individual batteries, for instance, $\boldsymbol{i}_{\mathrm{offset,misc}}$ can be adjusted to reduce the target current magnitude of the battery current $i_{\mathrm{bat},pm}$ and consequently reduce the load on the batteries in dependence of the temperature. Equation (7) shows a possible function to calculate each module's offset current $i_{\mathrm{offset,temp},pm}$ for temperature balancing. T_{pm} is the temperature of module m in phase p, the average temperature of all batteries is indicated with $\overline{T}$, the factor c can be calculated for normalization analogously to (4) and (5). g_temp is the factor how fast the temperatures shall be balanced. These module currents are summarized in the temperature offset current matrix $\boldsymbol{i}_{\mathrm{offset,temp}}$.

$$i_{\mathrm{offset,temp},pm} = -\frac{1}{c}(T_{pm} - \overline{T}) \cdot \sqrt{i_\mathrm{q,sp}^2 + i_\mathrm{d,sp}^2} \cdot g_\mathrm{temp} \quad (7)$$

Another option to define the target currents $\boldsymbol{i}_\mathrm{target}$ is to take the battery currents of the previous control cycle $\boldsymbol{i}_\mathrm{previous}$ into account to reduce the battery current ripple in consecutive cycles. It is also possible to explicitly define specific fixed target currents $\boldsymbol{i}_\mathrm{fixed}$ which shall be reached in the next modulation cycle to reduce microcycles of the battery.

D. Recuperation Detection

The recuperation detection checks whether the actual operating point allows recuperation. If the electrical power of the machine $P_\mathrm{machine,el}$ is negative, a recuperative operating point can be achieved. This binary information, derived from (8) is processed in the Target Current Calculation (TCC) block.

$$b_\mathrm{recup} = \begin{cases} 0 & \text{if } P_\mathrm{machine,el} \geq 0\,\mathrm{W} \\ 1 & \text{if } P_\mathrm{machine,el} < 0\,\mathrm{W} \end{cases} \quad (8)$$

E. Target Current Calculation

The block diagram of the TCC is illustrated in Fig. 4. With the MMSPC topology, it is possible to selectively discharge batteries in order to charge other batteries and thus equalize their respective SoCs. However, the charging and discharging currents inevitably result in ohmic losses in each of the batteries. Therefore, the batteries should only be actively charged at regenerative operating points, i.e. when recuperative braking is used. Therefore, the main operation strategy of TCM is to increase the load on charged batteries and to reduce it on discharged batteries. This can reduce not only the losses in the batteries, but also the charging cycles of the batteries. The currents from the efficiency, balancing and additional offset blocks are summed up and limited by a variable saturation afterwards. In motor operation mode, negative target currents are set to zero. The corresponding modules are neither loaded nor actively charged. As mentioned above, explicit charging

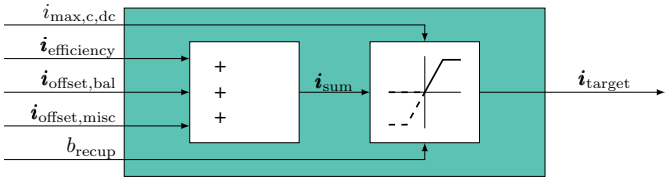

Fig. 4: Block diagram of TCC

currents are only allowed in recuperative operating points. In addition to the dynamic limitation, fixed maximum charging $i_{\mathrm{max,c}}$ and discharging $i_{\mathrm{max,dc}}$ currents limit the target currents $\boldsymbol{i}_{\mathrm{target}}$ to protect the batteries. The formal description of TCC including the variable saturation can be seen in (9) and (10).

$$\boldsymbol{i}_{\mathrm{sum}} = \boldsymbol{i}_{\mathrm{efficiency}} + \boldsymbol{i}_{\mathrm{offset,bal}} + \boldsymbol{i}_{\mathrm{offset,misc}} \tag{9}$$

$$i_{\mathrm{target},pm} = \begin{cases} i_{\mathrm{max,dc}} & \text{if } i_{\mathrm{max,dc}} \leq i_{\mathrm{sum},pm} \\ i_{\mathrm{sum},pm} & \text{if } 0\,\mathrm{A} \leq i_{\mathrm{sum},pm} < i_{\mathrm{max,dc}} \\ 0\,\mathrm{A} & \text{if } i_{\mathrm{sum},pm} < 0\,\mathrm{A} \wedge b_{\mathrm{recup}} = 0 \\ i_{\mathrm{sum},pm} & \text{if } i_{\mathrm{max,c}} < i_{\mathrm{sum},pm} < 0\,\mathrm{A} \wedge b_{\mathrm{recup}} = 1 \\ i_{\mathrm{max,c}} & \text{if } i_{\mathrm{sum},pm} \leq i_{\mathrm{max,c}} \wedge b_{\mathrm{recup}} = 1 \end{cases} \tag{10}$$

F. Cost Function

For each feasible switching state $\vec{s}_{\mathrm{feas}}$ which fulfills the calculated line-to-line voltages of the DSM for the next modulation step, the resulting battery currents $\boldsymbol{i}_{\mathrm{bat,pred}}$ are predicted, as explained in [17]. After calculating the battery currents $\boldsymbol{i}_{\mathrm{bat,pred}}$ for a specific switching vector $\vec{s}$, the sum of the squared deviations $J(\vec{s})$ of these predicted currents and the target currents $\boldsymbol{i}_{\mathrm{target}}$ is calculated as shown in (11).

$$J(\vec{s}) = \sum_{p=1}^{3} \sum_{m=1}^{n_{\mathrm{ph}}} \left(i_{\mathrm{target},pm} - i_{\mathrm{bat,pred},pm}(\vec{s})\right)^2 \tag{11}$$

The state vector $\vec{s}_{\mathrm{opt}}$ that minimizes the cost function $J(\vec{s})$ is selected and sent to the modules. The minimization of the objective function $J(\vec{s})$ can be seen in (12).

$$\begin{aligned} &\arg\min_{\vec{s}\in\vec{s}_{\mathrm{feas}}} J(\vec{s}) = \\ &= \arg\min_{\vec{s}\in\vec{s}_{\mathrm{feas}}} \left(\sum_{p=1}^{3} \sum_{m=1}^{n_{\mathrm{ph}}} \left(i_{\mathrm{target},pm} - i_{\mathrm{bat,pred},pm}(\vec{s})\right)^2 \right) \\ &= \vec{s}_{\mathrm{opt}} \end{aligned} \tag{12}$$

IV. Measurement Results

In order to proof TCM, it has been evaluated on a test bench. Tables I to IV show the system parameters of the used test environment. TCM is implemented on an MMSPC prototype with $n_{\mathrm{ph}} = 5$ modules per phase. Each module has an integrated lead-acid battery with a nominal voltage of $U_{\mathrm{bat,nom}} = 12\,\mathrm{V}$. A test bench with an automotive permanent magnet synchronous machine (PSM) and an ordinary industrial converter (SINAMICS S120) is used to emulate typical operation points of an EV. Therefore, to classify

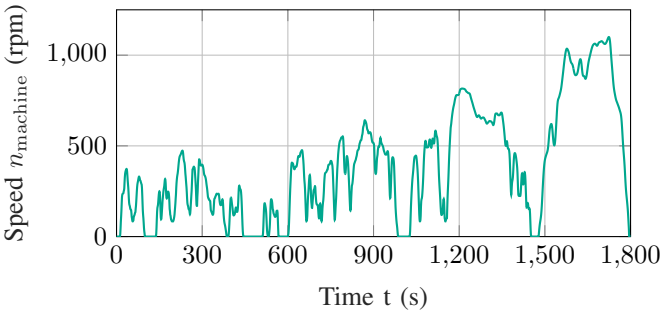

(a) Setpoints for machine speed n_{machine}

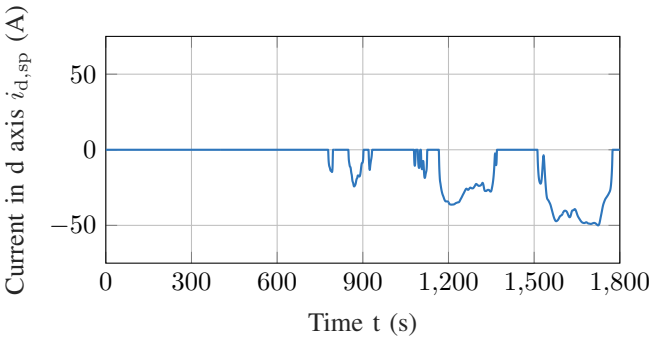

(b) Current setpoints in d axis $i_{\mathrm{d,sp}}$

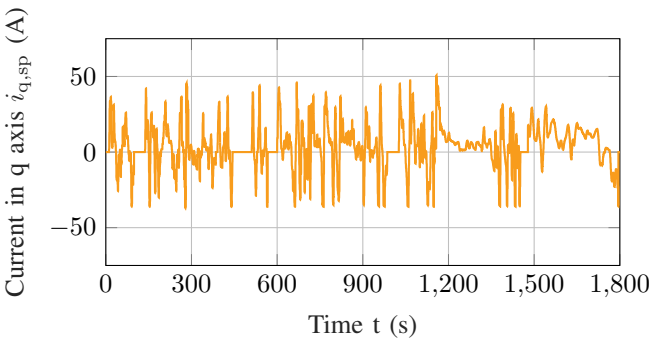

(c) Current setpoints in q axis $i_{\mathrm{q,sp}}$

Fig. 5: WLTP-Cycle class 3 setpoint values

TCM, the driving profile of a typical EV for the Worldwide Harmonized Light-Duty Vehicles Test Procedure (WLTP) class 3 driving cycle is used. Since the used MMSPC is a scaled prototype with valve-regulated lead-acid (VRLA) batteries with a nominal voltage of $U_{\mathrm{bat,nom}} = 12\,\mathrm{V}$, the resulting currents for generating torque and field-weakening have to be scaled according to the datasheet of the batteries, too. Fig. 5a shows the speed of the machine, Fig. 5b and Fig. 5c show the current setpoints for the d and q axis of the scaled WLTP. The operation points of the PSM during the WLTP are summarized in Table IV.The SoCs are estimated with an initial open-circuit voltage (OCV) measurement and a modified coulomb counting algorithm on each SM individually. The modification means that the measured battery currents for coulomb counting are

TABLE I
MMSPC parameters

Parameter	Symbol	Value
Control frequency MMSPC	f_{control}	80 kHz
Modules per phase	n_{ph}	5
Modulation frequency per phase	f_{mod}	80 kHz
MOSFET Drain-Source-resistance	$R_{\text{DS(on)}}$	4.4 mΩ

TABLE II
Battery parameters

Parameter	Symbol	Value
Battery Model		FGC21803
Nominal battery voltage	$U_{\text{bat,nom}}$	12 V
Battery capacity	C_{bat}	18 Ah
Battery resistance	R_{bat}	15 mΩ
Max. charging current	$i_{\text{max,c}}$	−1C = −18 A
Max. discharging current	$i_{\text{max,dc}}$	3C = 54 A

amplified by the factor 8. This equals a virtual reduction of the batteries' capacity by a factor of $\frac{1}{8}$ in order to have a visible change in the SoCs during one driving cycle. During the WLTP an overlaid system control unit sends new data for operation points for the MMSPC and the industrial machine every $t_{\text{op}} = 100\,\text{ms}$. The field-oriented current controllers for i_{d} and i_{q} for the MMSPC are implemented on a Cyclone IV EP4CE40F23C6 FPGA by Intel. Simultaneously, the industrial machine gets the setpoints for speed n_{machine} as reference.

It has to be mentioned that the resulting current combinations of $i_{\text{d,sp}}$ and $i_{\text{q,sp}}$ are not according to a loss minimizing algorithm of the PSM. They are scaled combinations of a typical automotive PSM during a WLTP to test different possible operation points of the MMSPC.

In order to compare different strategies, both the overall efficiency and the ability to balance the SoCs during a WLTP are used. To be able to compare different strategies, the starting SoCs of the batteries are set to 80 %. As indicator for efficiency the absolute change of the average SoC at the start $\overline{SoC}_{\text{start}}$ and the end $\overline{SoC}_{\text{end}}$ of a WLTP according to (13) is used. The deviation of the SMs' maximum and minimum SoC in the end

TABLE III
PSM parameters

Parameter	Symbol	Value
PSM pole pairs	p	16
PSM magnet flux linkage	ψ	37 mVs
PSM d-axis inductance	L_{d}	44 µH
PSM q-axis inductance	L_{q}	44 µH
PSM stator winding resistance	R_{s}	49.5 mΩ

TABLE IV
WLTP setpoints

Parameter	Symbol	Value
Setpoints machine speed	n_{machine}	0 rpm to 1100 rpm
Setpoint d-current	$i_{\text{d,sp}}$	−50 A to 0 A
Setpoint q-current	$i_{\text{q,sp}}$	−38 A to 50 A

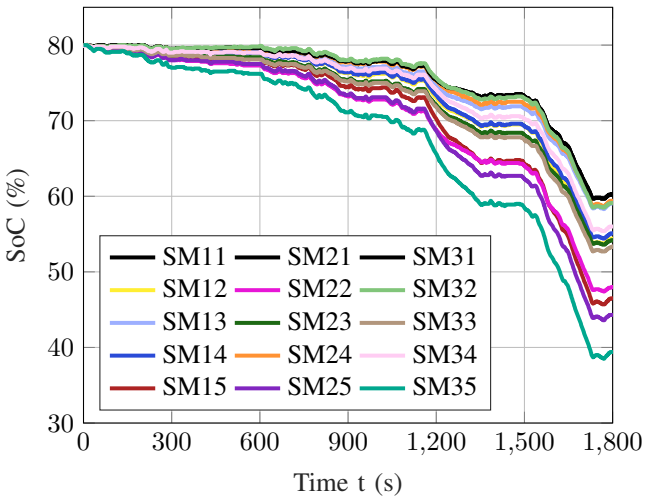

Fig. 6: SoCs during WLTP with focus on low internal ohmic losses with equal virtual starting SoCs of 80 % and without active balancing ($g_{\text{bal}} = 0$)

of the driving cycle $\Delta SoC_{\text{max,end}}$ is used as the indicator for the ability of balancing. It is calculated as shown in (14).

$$\Delta\overline{SoC} = \overline{SoC}_{\text{start}} - \overline{SoC}_{\text{end}} \tag{13}$$

$$\Delta SoC_{\text{max,end}} = \max\left(\boldsymbol{SoC}_{\text{end}}\right) - \min\left(\boldsymbol{SoC}_{\text{end}}\right) \tag{14}$$

As reference, without taking active balancing into account ($g_{\text{bal}} = 0$) and focusing on lowest internal resistance of the MMSPC only, the SoCs spread as shown in Fig. 6. As soon as the battery with the lowest SoC falls below a cut-off voltage (in this case SM35 which is the fifth SM in phase W), the operation area of the EV is restricted, even if other batteries are still charged. For reasons of symmetry and the macro topology of the MMSPC, the modules at the same position m in each phase p should have the same SoC. However, due to different aging and degradation states of the batteries, some are better or worse than others.

Figure 7 shows the SoCs during a WLTP while the only focus is set on balancing (i.e. $g_{\text{bal}} \gg 1$, efficient current distribution is neglected). Obviously, the SoCs do not diverge. As can be seen in Table V, the energy consumption and thus the value of $\Delta\overline{SoC}$ is higher in comparison to focusing on efficiency. As consequence, the driving range of an EV is lower than potentially possible, due to additional balancing losses.

These (Fig. 6 and Fig. 7) are examples for extreme parameter sets of g_{bal}. In contrast, even with modified, distributed starting SoCs, TCM with $0 < g_{\text{bal}} < 1$, leads to robust balancing behavior as shown in Fig. 8. Therefore in the end of a WLTP cycle, all batteries have an almost equal SoC and the operation of the EV is not restricted as long as there is still energy in the batteries left.

The SoCs shown in Fig. 8 are initialized to have high variation at $t = 0\,\text{s}$, verifying that balancing is ensured even in extreme cases. The initial average SoC of each phase is $\overline{SoC}_{\text{U}} = 78\,\%$, $\overline{SoC}_{\text{V}} = 66\,\%$ and $\overline{SoC}_{\text{W}} = 70\,\%$. It can

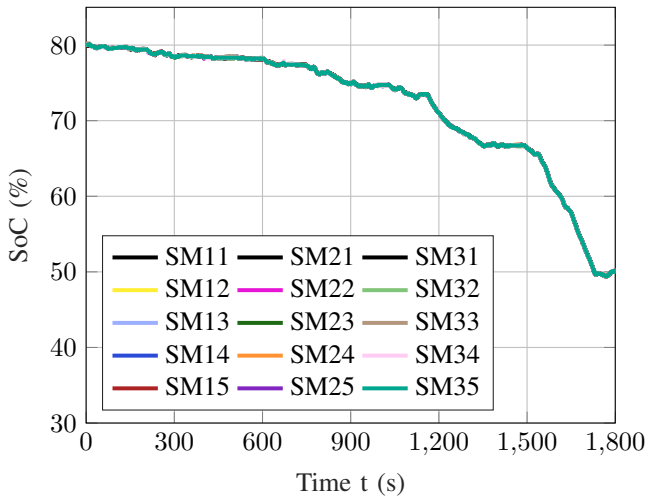

Fig. 7: SoCs during WLTP with only focus on SoC balancing ($g_{\mathrm{bal}} = 1000 \gg 1$) with virtual starting SoCs of 80 %

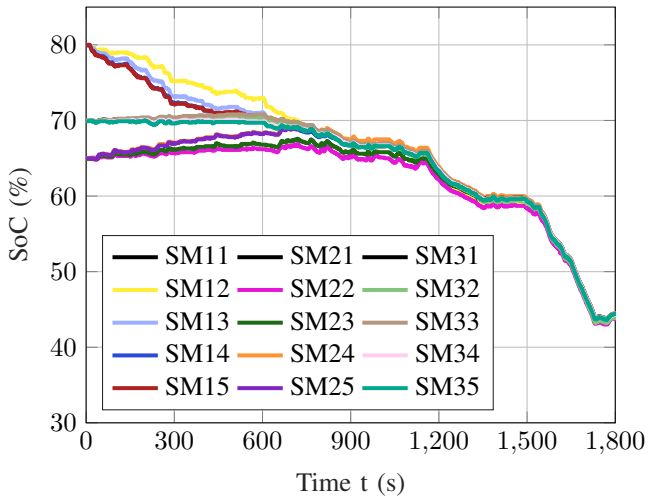

Fig. 8: SoCs during WLTP with TCM ($g_{\mathrm{bal}} = \frac{1}{4}$) with modified starting SoCs
($\overline{SoC}_{\mathrm{U}} = 78\,\%$, $\overline{SoC}_{\mathrm{V}} = 66\,\%$, $\overline{SoC}_{\mathrm{W}} = 70\,\%$)

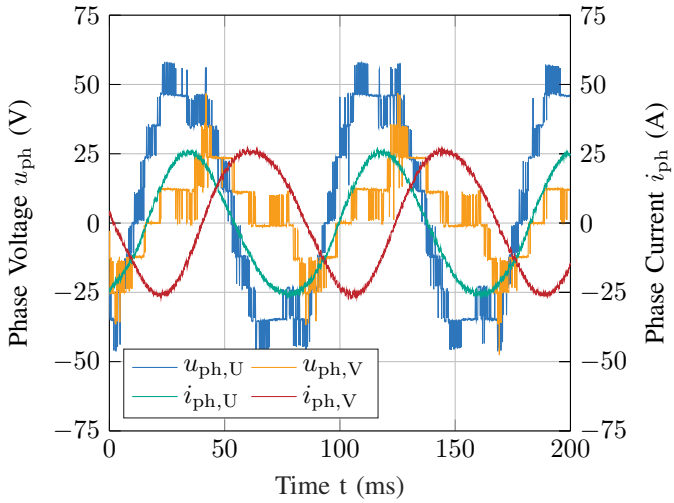

(a) Phase voltages and currents of phase U and V with TCM, phase W is not shown

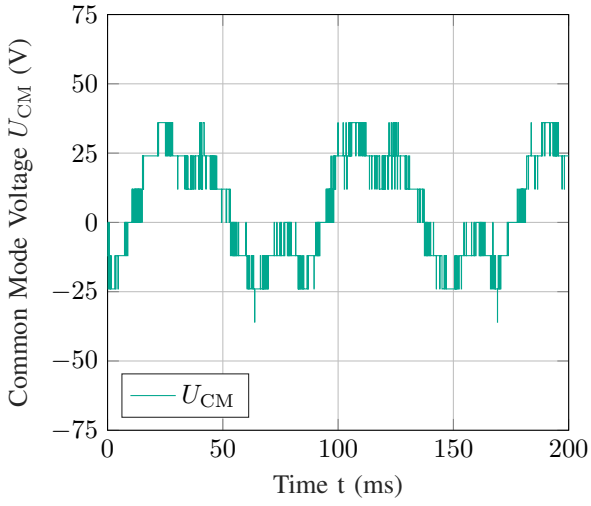

(b) Injected CM voltage U_{CM} due to TCM

Fig. 9: Phase voltages, currents and injected CM voltage with TCM ($\overline{SoC}_{\mathrm{U}} = 78\,\%$, $\overline{SoC}_{\mathrm{V}} = 66\,\%$, $\overline{SoC}_{\mathrm{W}} = 70\,\%$, $n_{\mathrm{machine}} = 450\,\mathrm{rpm}$, $i_{\mathrm{d}} = 0\,\mathrm{A}$, $i_{\mathrm{q}} = 25\,\mathrm{A}$)

be seen that after about $t = 1200\,\mathrm{s}$ the batteries are balanced, i.e. $\Delta\overline{SoC} < \pm 1\,\%\mathrm{P}$. In this particular case $g_{\mathrm{bal}} = \frac{1}{4}$ applies. In unmodified experiments, the initial SoCs are in the range of $\Delta\overline{SoC} < \pm 5\,\%\mathrm{P}$ of the average value $\overline{SoC}$ and they are balanced in less time.

Fig. 9a shows the voltages u_{ph} and currents i_{ph} of the phases U and V of the MMSPC at the operation point $n_{\mathrm{machine}} = 450\,\mathrm{rpm}$, $i_{\mathrm{d}} = 0\,\mathrm{A}$ and $i_{\mathrm{q}} = 25\,\mathrm{A}$ with the same SoC-deviation as shown in Fig. 8 at $t = 0\,\mathrm{s}$. For simplified visualization, phase W is not shown in Fig. 9a because it does not provide any further information.

As expected for PSMs, it can be seen that the phase currents $i_{\mathrm{ph,U}}$ and $i_{\mathrm{ph,V}}$ (purple and green) are shifted by 120°. However, the phase voltages (blue and red) are neither shifted nor symmetrical. This is caused by the injected CM voltage U_{CM} as shown in Fig. 9b. The CM voltage U_{CM} seems to be a superposition of mainly two waves. Besides a small third harmonic CM voltage to reduce conduction losses, comparable to the main result in [15], there is a fundamental wave that is synchronous to the phase voltage $u_{\mathrm{ph,U}}$. This is caused by the TCM algorithm to balance the SoCs. Through increasing the amplitude of a higher charged phase, more SMs are connected in series, therefore more batteries are loaded with the respective phase current i_{ph}. At the same time, this CM voltage reduces the amplitude of the other phases which leads to the possibility to have more SMs in parallel. As a result, the load of the batteries of these SMs is reduced.

Quantitative results of the new approach and the comparison to a reference algorithm according to [17] are shown in Table V.

Since a single discharged battery leads to a reduction in the operation area of the MMSPC and also prohibits using the parallel states due to high equalizing currents, balancing of

TABLE V
Measured results with WLTP

Method	$\Delta\overline{SoC}$	$\Delta SoC_{\max,\mathrm{end}}$
TCM Efficiency (Fig. 6)	26.0 %P	21.0 %P
Reference Balancing (Fig. 7)	29.9 %P	0.2 %P
TCM Combination (Fig. 8)	27.0 %P	0.8 %P

the batteries while being in operation is crucial. Therefore, taking only efficiency into account (as shown in Fig. 6) does not provide a reliable operation mode over the full operational range. If only balancing is taken into account additional charging and discharging losses reduce the energy of the batteries which could be used for propulsion of the EV. The TCM algorithm with both low losses and active balancing leads to a good trade-off as shown in Fig. 8. It has slightly higher losses than the algorithm without active balancing but is able to balance the SoCs at the same time.

V. Conclusion

In this paper a new real-time algorithm to combine high efficient operation and active balancing for MMSPCs is introduced. The developed TCM method uses the loss optimal current distribution together with the SoC to achieve high efficiency while balancing the batteries actively during a WLTP class 3 driving cycle. On top of that, the method can easily be extended with other objectives like thermal balancing, fixed target currents and battery current ripple control. Experimental results on a test bench with an automotive test cycle validate the robust and reliable performance of TCM. Even with extreme SoCs in the beginning of a WLTP, balancing is ensured and the deviation at the end of a WLTP is $\Delta SoC_{\max,\mathrm{end}} < 1\,\%\mathrm{P}$ while having only slightly higher $\Delta\overline{SoC}$ in comparison to focusing on high efficiency only.

References

[1] A. Lesnicar and R. Marquardt, "An innovative modular multilevel converter topology suitable for a wide power range," *2003 IEEE Bologna PowerTech - Conference Proceedings*, vol. 3, pp. 6–11, 2003. DOI: 10.1109/PTC.2003.1304403.

[2] H. Akagi, S. Inoue, and T. Yoshii, "Control and performance of a transformerless cascade PWM STATCOM with star configuration," *IEEE Transactions on Industry Applications*, vol. 43, no. 4, pp. 1041–1049, 2007, ISSN: 00939994. DOI: 10.1109/TIA.2007.900487.

[3] R. Lizana F., S. Rivera, Z. Li, *et al.*, "Modular Multilevel Series/Parallel Converter for Bipolar DC Distribution and Transmission," *IEEE Journal of Emerging and Selected Topics in Power Electronics*, vol. 9, no. 2, pp. 1765–1779, 2020, ISSN: 2168-6777. DOI: 10.1109/jestpe.2020.2998738.

[4] J. Asakura and H. Akagi, "State-of-Charge (SOC)-Balancing Control of a Battery Energy Storage System Based on a Cascade PWM Converter," *IEEE Transactions on Power Electronics*, vol. 24, no. 6, pp. 1628–1636, 2009, ISSN: 19410107. DOI: 10.1109/TPEL.2009.2014868.

[5] F. Helling, S. Gotz, and T. Weyh, "A battery modular multilevel management system (BM3) for electric vehicles and stationary energy storage systems," *2014 16th European Conference on Power Electronics and Applications, EPE-ECCE Europe 2014*, 2014. DOI: 10.1109/EPE.2014.6910821.

[6] M. Malinowski, K. Gopakumar, J. Rodriguez, and M. A. Perez, "A survey on cascaded multilevel inverters," *IEEE Transactions on Industrial Electronics*, vol. 57, no. 7, pp. 2197–2206, 2010, ISSN: 02780046. DOI: 10.1109/TIE.2009.2030767.

[7] J. Kolb, F. Kammerer, M. Gommeringer, and M. Braun, "Cascaded control system of the modular multilevel converter for feeding variable-speed drives," *IEEE Transactions on Power Electronics*, vol. 30, no. 1, pp. 349–357, 2015, ISSN: 08858993. DOI: 10.1109/TPEL.2014.2299894.

[8] F. Helling, J. Gluck, A. Singer, and T. Weyh, "Modular multilevel battery (M2B) for electric vehicles," *2016 18th European Conference on Power Electronics and Applications, EPE 2016 ECCE Europe*, 2016. DOI: 10.1109/EPE.2016.7695480.

[9] C. Korte, E. Specht, M. Hiller, and S. Goetz, "Efficiency evaluation of MMSPC/CHB topologies for automotive applications," in *Proceedings of the International Conference on Power Electronics and Drive Systems*, vol. 2017-Decem, Institute of Electrical and Electronics Engineers Inc., Feb. 2018, pp. 324–330, ISBN: 9781509023646. DOI: 10.1109/PEDS.2017.8289145.

[10] A. Kersten, M. Kuder, E. Grunditz, *et al.*, "Inverter and battery drive cycle efficiency comparisons of CHB and MMSP traction inverters for electric vehicles," *2019 21st European Conference on Power Electronics and Applications, EPE 2019 ECCE Europe*, pp. 1–12, 2019. DOI: 10.23919/EPE.2019.8915147.

[11] S. M. Goetz, A. V. Peterchev, and T. Weyh, "Modular multilevel converter with series and parallel module connectivity: Topology and control," *IEEE Transactions on Power Electronics*, vol. 30, no. 1, pp. 203–215, 2015, ISSN: 08858993. DOI: 10.1109/TPEL.2014.2310225.

[12] Z. Li, R. Lizana, A. V. Peterchev, and S. M. Goetz, "Distributed balancing control for modular multilevel series/parallel converter with capability of sensorless operation," *2017 IEEE Energy Conversion Congress and Exposition, ECCE 2017*, vol. 2017-Janua, no. 1608929, pp. 1787–1793, 2017. DOI: 10.1109/ECCE.2017.8096011.

[13] Z. Li, R. Lizana, A. V. Peterchev, and S. M. Goetz, "Predictive control of modular multilevel series/parallel converter for battery systems," in *2017 IEEE Energy Conversion Congress and Exposition, ECCE 2017*, vol. 2017-Janua, Institute of Electrical and Electronics Engineers Inc., Nov. 2017, pp. 5685–5691, ISBN: 9781509029983. DOI: 10.1109/ECCE.2017.8096945.

[14] E. Specht, C. Korte, and M. Hiller, "Reducing computation effort by parallel optimization for modular multilevel converters," in *Proceedings: IECON 2018 - 44th Annual Conference of the IEEE Industrial Electronics Society*, Institute of Electrical and Electronics Engineers Inc., Dec. 2018, pp. 3991–3996, ISBN: 9781509066841. DOI: 10.1109/IECON.2018.8591496.

[15] C. Korte, E. Specht, S. M. Goetz, and M. Hiller, "A Control Scheme to Reduce the Current Load of Integrated Batteries in Cascaded Multilevel Converters," *ICPE 2019 - ECCE Asia - 10th International Conference on Power Electronics - ECCE Asia*, 2019. DOI: 10.23919/icpe2019-ecceasia42246.2019.8797109.

[16] C. Wang, A. V. Peterchev, and S. M. Goetz, "Closed-loop predictively optimizing control for modular multilevel converter with parallel connectivity," *2019 21st European Conference on Power Electronics and Applications, EPE 2019 ECCE Europe*, pp. 1–10, 2019. DOI: 10.23919/EPE.2019.8915103.

[17] T. Merz, C. Korte, E. Specht, and M. Hiller, "Optimizing Utilization of an MMSPC with Model Predictive Control," *2020 IEEE 21st Workshop on Control and Modeling for Power Electronics, COMPEL 2020*, 2020. DOI: 10.1109/COMPEL49091.2020.9265803.

[18] D. Kraus, E. Specht, T. Merz, and M. Hiller, "Optimized real-time control for modular multilevel converters using adaptive neural networks," *2019 21st European Conference on Power Electronics and Applications, EPE 2019 ECCE Europe*, 2019. DOI: 10.23919/EPE.2019.8915464.